JGR Space Physics

RESEARCH ARTICLE
10.1029/2023JA031587

Key Points:

- Transient-large-amplitude (TLA) magnetic field disturbances were most common during the declining phase of Solar Cycle 24
- A majority of extreme nighttime geomagnetic disturbances (GMDs) from 2015 to 2019 had TLA intervals that preceded or occurred within the GMD
- TLA-related GMDs are related to inner magnetosphere dipolarizations, subsequent poleward boundary intensifications, and auroral streamers

Supporting Information:

Supporting Information may be found in the online version of this article.

Correspondence to:

B. A. McCuen,
bmccuen@umich.edu

Citation:

McCuen, B. A., Moldwin, M. B., Engebretson, M. J., Weygand, J. M., & Nishimura, Y. (2023). Magnetosphere–ionosphere drivers of transient-large-amplitude geomagnetic disturbances: Statistical analysis and event study. *Journal of Geophysical Research: Space Physics*, *128*, e2023JA031587. https://doi.org/10.1029/2023JA031587

Received 12 APR 2023
Accepted 27 OCT 2023

Magnetosphere–Ionosphere Drivers of Transient-Large-Amplitude Geomagnetic Disturbances: Statistical Analysis and Event Study

Brett A. McCuen[1], Mark B. Moldwin[1], Mark J. Engebretson[2], James M. Weygand[3], and Yukitoshi Nishimura[4]

[1]Department of Climate and Space Sciences and Engineering, University of Michigan, Ann Arbor, MI, USA, [2]Department of Physics, Augsburg University, Minneapolis, MN, USA, [3]Department of Earth, Planetary, and Space Sciences, University of California, Los Angeles, CA, USA, [4]Department of Electrical and Computer Engineering, Center for Space Physics, Boston University, Boston, MA, USA

Abstract We present a comprehensive statistical analysis of high-frequency transient-large-amplitude (TLA) magnetic perturbation events that occurred at 12 high-latitude ground magnetometer stations throughout Solar Cycle 24 from 2009 to 2019. TLA signatures are defined as one or more second-timescale d*B*/d*t* interval with magnitude ≥6 nT/s within an hour event window. This study characterizes high-frequency TLA events based on their spatial and temporal behavior, relation to ring current activity, auroral substorms, and nighttime geomagnetic disturbance (GMD) events. We show that TLA events occur primarily at night, solely in the high-latitude region above 60° geomagnetic latitude, and commonly within 30 min of substorm onsets. The largest TLA events occurred more often in the declining phase of the solar cycle when ring current activity was lower and solar wind velocity was higher, suggesting association to high-speed streams caused by coronal holes and subsequent corotating interaction regions reaching Earth. TLA perturbations often occurred preceding or within the most extreme nighttime GMD events that have 5–10 min timescales, but the TLA intervals were often even more localized than the ∼300 km effective scale size of GMDs. We provide evidence that shows TLA-related GMD events are associated with dipolarization fronts in the magnetotail and fast flows toward Earth and are closely temporally associated with poleward boundary intensifications (PBIs) and auroral streamers. The highly localized behavior and connection to the most extreme GMD events suggests that TLA intervals are a ground manifestation of features within rapid and complex ionospheric structures that can drive geomagnetically induced currents.

Plain Language Summary Large changes of the surface geomagnetic field can drive geomagnetically induced currents (GICs) that are a hazardous impact of space weather events. Extreme magnetic field changes with timescales of minutes and hours are the most dangerous because they are the most effective at inducing currents on Earth. Shorter-period geomagnetic disturbances are less effective at current induction, but we show in this study that they are inherently related to and play an active role in space weather events that are capable of driving GICs. We analyze these high-frequency events that occurred at stations in the high-magnetic latitude region throughout Solar Cycle 24 and investigate their association to longer (5–10 min) geomagnetic disturbances that can cause GICs. We show that they are often closely correlated and that the associated events can be driven by bursty flows in the magnetotail and subsequent small-scale auroral structures.

1. Introduction

Extreme space weather events like geomagnetic storms and substorms can drive large geomagnetically induced currents (GICs) through conductors on Earth's surface. GICs pose a significant threat to technological infrastructure as they can result in costly equipment damage and power outages (Boteler et al., 1998; A. Pulkkinen et al., 2017). For decades, GICs have been studied with various methods in order to forecast their occurrence and mitigate their consequences. From Faraday's law of induction, the induced currents on the ground are directly related to large changes of the surface geomagnetic field, and thus the magnetic field changes—d*B*/d*t*—are often studied as proxy for GICs, though it is the surface geoelectric field and ground conductivity structure that determines the size of the GIC.

The largest and longest space weather events are generally considered to pose the greatest threat to technological infrastructure. These events typically cause geomagnetic field disturbances that last from tens of minutes to several hours and have peak derivative amplitudes exceeding 8 nT/s (Kappenman, 2006). However, recent studies have shown that more rapid and localized processes are also capable of generating GICs (Engebretson et al., 2019a, 2021; Ngwira et al., 2015; A. Pulkkinen et al., 2015). Case studies of some of these processes were presented by Belakhovsky et al. (2019) and include sudden commencements (SCs), dayside traveling convection vortices (TCVs), nightside geomagnetic disturbance (GMD) events, and irregular Pi 3 pulsations. All of these space weather processes have timescales of 1–10 min and frequency range of 1–22 mHz.

Higher-frequency Pi 1 and Pi 2 magnetic pulsations with irregular waveforms and periods of 1–40 and 40–150 s, respectively (Jacobs et al., 1964), have long been studied for their role in substorm dynamics. Pi2 waves are commonly associated with the development substorm current wedge (SCW; Atkinson, 1967; McPherron et al., 1973); the polarizations of Pi 2 magnetic pulsations on the ground have been used to identify the location of the SCW (Lester et al., 1983). Pi 1 pulsations have also been observed in association with substorm onsets (Lessard et al., 2006) and have been shown to be caused by local ionospheric enhancements and particle precipitation (Arnoldy et al., 1987; Engebretson et al., 1983).

While type Pi 1–2 magnetic pulsations are clearly associated with substorm processes, disturbances with these frequencies are not generally associated with GIC activity. Magnetic perturbations in the Pi 1–2 frequency range with second timescales are less studied in the context of GICs as they are incapable of directly driving large currents through conductors on the surface of Earth. However, it has been shown recently that magnetic field perturbations in this frequency range are an important aspect of larger space weather events that can cause GICs.

McCuen et al. (2021) found that high-frequency transient-large-amplitude (TLA) dB/dt intervals (17–1,000 mHz; 1–60 s periods) with derivative amplitude greater than 6 nT/s often occur prior to or within many of the most intense nighttime GMD events that could drive GICs. Any number of TLA dB/dt intervals that occur within a one-hour window at a single station location are referred to collectively as a TLA event. Nighttime GMDs are large, isolated geomagnetic perturbations with overall amplitudes of hundreds of nanotesla and 5–10 min periods (Engebretson et al., 2019a). These events are often associated with substorm onsets but do not require substorm activity to occur (Engebretson et al., 2021).

It is shown in McCuen et al. (2021) that TLA dB/dt intervals are often related to nighttime GMDs and auroral substorms; however, this relationship is complex. TLA dB/dt with Pi 1–2 pulsation periods are sometimes involved in substorm processes but do not always occur in close temporal proximity to substorm onsets or geomagnetic storms. While SCs have been previously thought to be a primary driver for the most rapid and large-amplitude magnetic field perturbations (Kataoka & Ngwira, 2016), there was only one SC-related TLA event despite five other SC events that occurred in 2015 while the stations were located on the dayside. Rather than SCs and large geomagnetic storms, the largest TLA events were most often associated with smaller-scale processes like GMDs and substorms, suggesting that small-scale ionospheric currents are involved in driving these large-amplitude, high-frequency signatures.

These high-frequency TLA magnetic field intervals show a clear relation to other GIC-causing space weather events; however, the exact role these variations play within and in association to larger events is yet unknown. The goals of this study are to (a) more broadly understand the behavior of TLA events throughout the solar cycle, (b) more clearly define how high-frequency perturbations behave within larger space weather events, especially nighttime GMDs, and (c) determine the small-scale ionospheric currents and space weather phenomena that give rise to these disturbances. We analyze TLA dB/dt events in magnetometer data from multiple arrays that span the high-latitude region of North America and throughout Solar Cycle 24. We discuss these events in the context of other space weather phenomena and suggest possible physical mechanisms for their generation based on the evidence presented.

2. Data

The data used in this study are from multiple magnetometer arrays. Table 1 gives the geographic and corrected geomagnetic (CGM) coordinates for the stations as well as the array each station is a part of; the map shown in Figure 1 shows the locations of these stations in CGM coordinates. The details of each array and instrumentation

Table 1
Location Coordinates of Stations Used in This Study

Station code	Geographic latitude	Geographic longitude	Corrected geomagnetic latitude	Corrected geomagnetic longitude	Observatory system	UT of magnetic local midnight
IGL	69.3	278.2	77.7	354.9	MACCS	05:09
GJO	68.6	264.2	76.9	328.48	MACCS	06:42
RBY	66.5	273.8	75.3	347	MACCS	05:38
PGG	66.1	294.2	73.3	19.9	MACCS	03:37
CDR	64.2	283.4	72.6	2.9	MACCS	04:40
RANK	62.8	267.7	71.8	337.4	CARISMA	06:13
SALU	62.2	284.4	70.8	4.0	AUTUMNX	04:35
YKC	62.48	245.5	68.9	304	CANMOS	08:22
FCC	58.8	265.9	67.85	334.9	CANMOS	06:22
GILL	56.4	265.3	65.5	334.3	CARISMA	06:24
WHIT	61.01	224.8	63.5	281	THEMIS GBO	09:57
KJPK	55.3	282.2	62.4	359.9	AUTUMNX	04:50
ATHA	54.71	246.7	61.5	308.5	CARISMA	08:04
MEA	54.62	246.7	61.44	308.43	CANMOS	08:04

Note. The CGM coordinates were calculated using the AACGM-v2 Calculator (available at http://sdnet.thayer.dartmouth.edu/aacgm/aacgm_calc.php#AACGM) for epoch 2014. Note epoch 2014 was used as it is the median year of Solar Cycle 24.

are outlined below. It is important to note that we also surveyed 10 stations located in the midlatitude and equatorial regions and no TLA events were identified below 61° magnetic latitude.

1. The Magnetometer Array for Cusp and Cleft Studies (MACCS) is a system of magnetometers located in north-east Nunavut, Canada from about 65° to 80° geomagnetic latitude (Engebretson et al., 1995). MACCS is operated by Augsburg University and the University of Michigan and is funded by the National Science Foundation (NSF). The MACCS stations contain fluxgate magnetometers with axes aligned with the Earth's

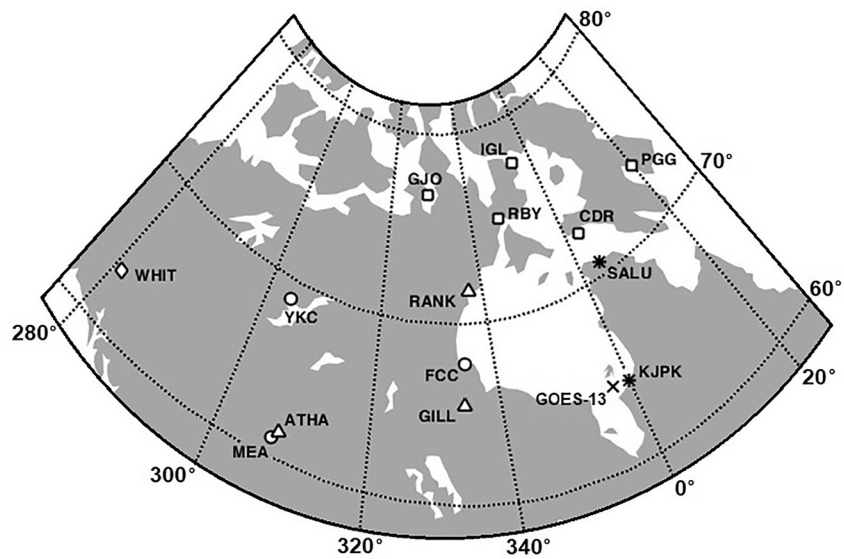

Figure 1. Locations of the magnetometer stations used in this study. The symbols for each station represent the array to which they belong: squares signify MACCS stations, triangles signify CARISMA stations, circles are for CANMOS stations, the diamond is for the THEMIS GBO, and the asterisks represent AUTUMNX stations. The X marks the magnetic footprint of the GOES-13 spacecraft (determined using tools from SSCWEB https://sscweb.gsfc.nasa.gov/) during the event discussed in Section 7. Lines of the latitude and longitude are shown in corrected geomagnetic coordinates for epoch 2014.

magnetic field (*H*: magnetic north-south, *D*: east-west, *Z*: vertical with positive direction downward into Earth). The MACCS magnetometers measure the magnetic field at 8 Hz and then average and record the measurements at 2 Hz (half-second cadence); the measurements are accurate to 0.025 nT.

2. The Canadian Array for Realtime InvestigationS of Magnetic Activity (CARISMA) is a system of ground-based magnetometers located across central Canada (Mann et al., 2008). CARISMA is operated by the University of Alberta as part of the Canadian Geospace Monitoring Program (CGSM) and is funded by the Canadian Space Agency (CSA). Like MACCS, the CARISMA system consists of fluxgate magnetometers that measure the magnetic field at eight samples/s. The stations used in this study offer final data products that are averaged to two samples/s and rotated from the geographic coordinates they are originally measured in to local geomagnetic coordinates. These magnetometer systems offer 0.025 nT resolution data.
3. The CANadian Magnetic Observatory System (CANMOS; Nikitina et al., 2016) is a ground magnetometer array operated by Natural Resources Canada (NRCan). CANMOS employs fluxgate magnetometers across Canada that sample the magnetic field at 8 Hz, then resamples to 1 Hz after despiking and performing a nine-point rectangular filter. The CANMOS data have 0.01 nT resolution. The data from CANMOS are in geographic coordinates: *x* (geographic north-south), *y* (geographic east-west), and *z* (vertical).
4. The Athabasca University Time History of Events and Macroscale Interactions During Substorms (THEMIS) University of California, Los Angeles (UCLA) Magnetometer Network eXtension (AUTUMNX; Connors et al., 2016) is located in the eastern region of Canada. The AUTUMNX instruments are fluxgate magnetometers provided by UCLA that measure the magnetic field with 0.01 nT resolution at two samples/s and in local geomagnetic coordinates.
5. THEMIS Ground-Based Observatory (GBO) systems (Russell et al., 2008) are a part of the larger collaboration of stations that contribute magnetic data to the THEMIS Ground Magnetometer (GMAG) cooperative. THEMIS GBO stations are operated by UCLA, contain UCLA instruments as in (4), and thus have the same resolution, measurement frequency, and coordinate system as mentioned above.

3. Methodology

A high-frequency TLA event is defined as a 1-hr period at a single station in which there is at least one dB/dt interval with timescale from 2 to 60 s and magnitude greater than 6 nT/s (subsequent $\Delta B > 60$ nT). The lower derivative amplitude threshold of 6 nT/s was chosen as it is comparable to the 8 nT/s disturbances observed during the geomagnetic storm of March 1989 that caused significant power system damage (Kappenman, 2006). Note that GMDs during storms persist for timescales much longer than 60 s, but the 6 nT/s threshold serves as a baseline for what is considered to be large dB/dt.

TLA events often present as clusters of these dB/dt intervals in multiple components of the magnetic field data at a given station. An example of a TLA event is shown in the bottom panel of Figure 2, showing magnetic field data for ∼1 hr at the RANK station on 17 December 2017. The specific TLA dB/dt intervals are marked near 06:10 UT with the open circles (start of the interval) and closed circles (end of the interval) in each component. This TLA event occurred within an overall nighttime GMD event that began around 06:05 UT and peaked at about 06:15 UT.

The other station data are shown in the panels above RANK in Figure 2 because they show nighttime GMD events from about 06:10 to 06:20 UT as well as 06:30 to 06:40 UT (Engebretson, 2023). The GMDs at both RBY and CDR have maximum derivative amplitudes exceeding 10 nT/s. There is also a nighttime GMD that occurred at RANK beginning at about 06:05 UT. The RANK station measured TLA dB/dt that also exceeded 10 nT/s, and the overall magnetic field change during the entire interval was largest at RANK, with ΔBz of nearly 800 nT from 06:09 to 06:15.

In order to identify instances of TLA events in ground magnetic field data, an automated dB/dt search procedure was designed. The automated procedure is necessary because the characteristics of TLA dB/dt intervals are very similar to that of magnetometer "noise," referred to in this study as signals resulting from outside interference or instrumentation error that do not have geophysical sources. Noise-type signals in magnetometer data are often very short-timescale and large-amplitude dB/dt intervals, so identifying TLA signatures and distinguishing them from noise-type signals is an imperative aspect of this research.

The automated GMD classifier is described thoroughly in McCuen (2023) and discussed briefly here. The basic algorithm functions by partitioning every hour of data consecutively based on the number of data points and the

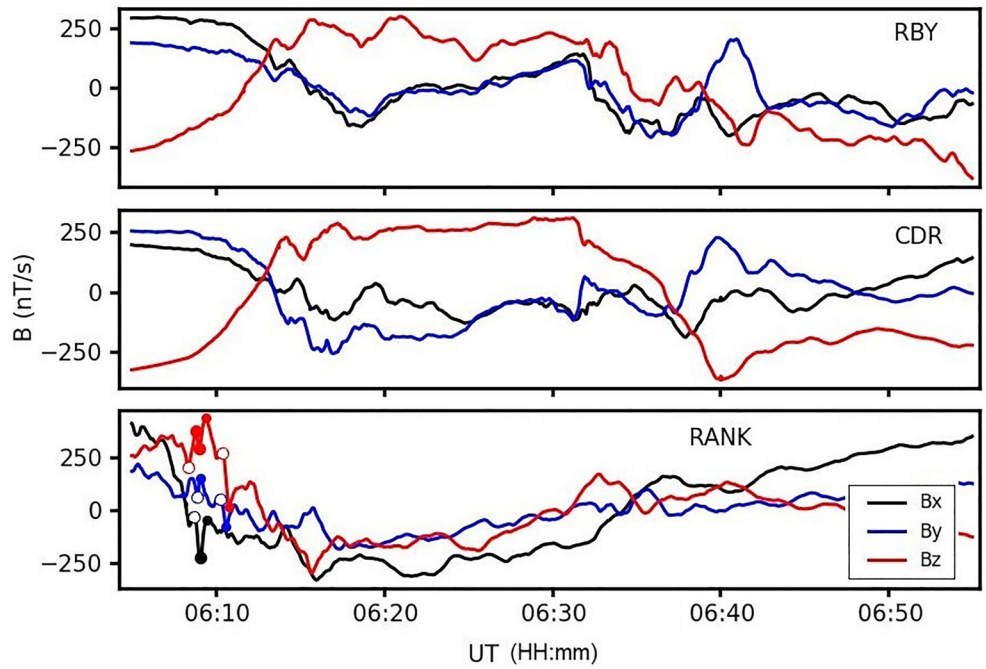

Figure 2. Magnetic field data from three stations on 17 December 2017. The Bx-component is displayed in black, By in blue, and Bz in red. The transient-large-amplitude (TLA) intervals are signified by hollow circles denoting the start of the interval and filled circles denoting the end of the interval. The mean *B* value in the each component has been subtracted.

measurement frequency (i.e., for the 2 Hz MACCS data, the first hour partition is the first 7,200 data points and the second hour partition is the following 7,200 data points). Then, instances where the sign of the slope of the magnetic field changes and remains the same for at least two measurement cycles (i.e., for 1 consecutive second for 2 Hz data or 2 s for 1 Hz data) are identified. The consistency of sign change for two cycles is required to reduce single-point errors/spikes in the data or highly variable data due to noise interference.

After the slope sign changes are identified, the time difference between each slope sign change is calculated (i.e., the Δt between each change of slope direction) as well as the change in magnetic field strength (ΔB), and the rate-of-change of the interval (dB/dt). Finally, this first step of the process identifies all of the intervals between changes of the sign of the slope that last from 1 to 60 s and have rate-of-change of at least |6| nT/s.

The next steps of the algorithm incorporate a filtering process that has requirements derived from the statistical analysis of geophysical and noise-type events described in McCuen et al. (2023). The first condition is that at least one dB/dt interval identified from the first step in each hour window of data lasts 10 s or more. This condition is defined because all of the geophysical events identified in the MACCS data for 2015 met this criteria, whereas a large number of hour windows with only noise-type dB/dt exhibited only intervals that lasted less than 10 s. If any dB/dt identified in an hour window lasts more than 10 s and has derivative amplitude of at least |6|, the ratio filter is performed.

This ratio filter finds the ratio of the number second-timescale $dB/dt > 6$ nT/s to the total number of dB/dt intervals within the hour (in which the magnetic field changes for at least two measurement cycles, for any timescale and magnitude). If this ratio is less than 5%, then the dB/dt intervals identified in the hour advance to the next step in the process. This condition is implemented because many noise-type events in magnetometer data consist of more than 5% concentration of large, second-timescale dB/dt (hundreds, sometimes thousands of dB/dt within an hour period), so this ratio filter excludes instances that are highly likely to be a result of noise interference rather than geophysical source. The 5% ratio threshold is another requirement derived from the analysis of McCuen et al. (2023).

Finally, if the first two qualifiers are met (i.e., if there are second-timescale $dB/dt > 6$ nT/s intervals and at least one interval with 10–60 s timescale, and the 5% ratio filter is passed), then a support vector machine (SVM) classification is performed on the dB/dt intervals to classify them as either geophysical TLA or noise type. The

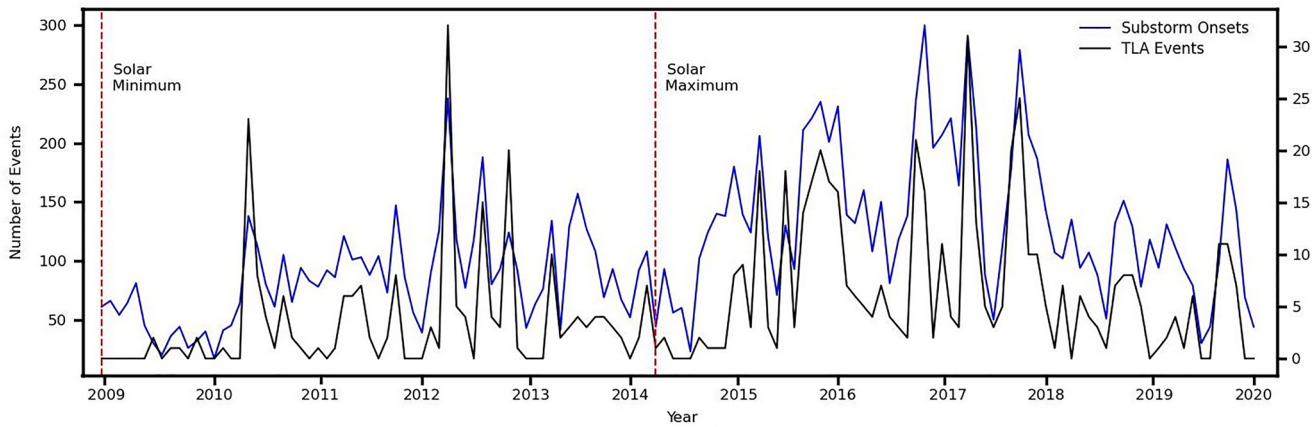

Figure 3. Number of substorm events (blue) and transient-large-amplitude (TLA) events (black) per month from late 2009 to early 2020. Values are plotted with separate *y*-axes: the left *y*-axis shows the number of substorm onsets and the right *y*-axis gives the number of TLA events.

SVM classification is performed on the dB/dt intervals within the hour window and the majority vote of these individual classifications is assigned to all of the dB/dt intervals within the hour. Then, if the SVM classifies a majority of the dB/dt intervals as TLA, they are returned as a data product.

4. Solar Cycle Dependence of TLA Events

In this section, a subset of stations was selected to examine the solar cycle dependence of TLA events. This subset excludes TLA event data from the MACCS stations as well as KJPK and SALU. These stations were selected because there is more uniform data availability throughout the solar cycle (see Table S1 in Supporting Information S1 for yearly data availability). The analysis in this section and the figures shown use this subset of events.

To explore the occurrence of TLA events in comparison to both sunspots and substorms throughout Solar Cycle 24, we reference Figure 3: the number of substorms per month from late 2009 to 2020 (shown in blue) and the number of TLA events per month (shown in black). The number of substorm onsets is from the SuperMAG substorm event list (Newell & Gjerloev, 2011); this method defines substorm onset as the initial minute in which the SML index drops sharply by 45 nT in the next 3 min and has a sustained negative bay of at least 100 nT over the following half-hour. The SML index is the lower envelope of N-component magnetic field measurements at stations between 40° and 80° magnetic north and reflects the maximum strength of the westward auroral electrojet. This index makes up half of the overall SuperMAG electrojet index, SME, derived by subtracting the SML values from the upper-envelope of N-component values (SMU) from the same set of stations. In Figure 3, the vertical red dashed lines show the times of Solar Minimum and Maximum for Solar Cycle 24 (note that the following Solar Minimum was in April 2020, just beyond the range shown in Figure 3). Figure 3 shows that while the number of TLA events throughout a 1-month period is much fewer than substorm onsets, TLA events often occurred in higher numbers when substorm onsets also occurred more often in a given month. Further, this figure also shows that both TLA events and substorm onsets increased during the declining phase of the solar cycle from mid-2014 to 2019.

Next, the association of TLA event occurrences to ring current activity and solar wind speed throughout the solar cycle is examined. Figure 4a displays the probability density of all SuperMAG ring (SMR) current index (Newell & Gjerloev, 2012) values for 2009–2019 (shown in red) compared with the SMR values during the minute of the maximum dB/dt interval of each TLA events from 2009 to 2019. Figure 4a shows that SMR values have a narrow distribution that peaks near zero with average value of −6 nT and standard deviation (σ) of ∼15 nT, while the distribution for TLA events is shifted to more negative values, peaking from 0 to −50 nT (mean value of −54 nT) with a larger σ of 43 nT and a long tail that extends to −175 nT. While a majority of TLA events occur for only slightly elevated SMR values, this distribution shows that some TLA events are related to very active geomagnetic storms.

Figure 4b shows the probability distribution of all solar wind flow speed values, Vsw, for every minute throughout the solar cycle (red) compared with the solar wind flow speed during the minute of the maximum dB/dt interval

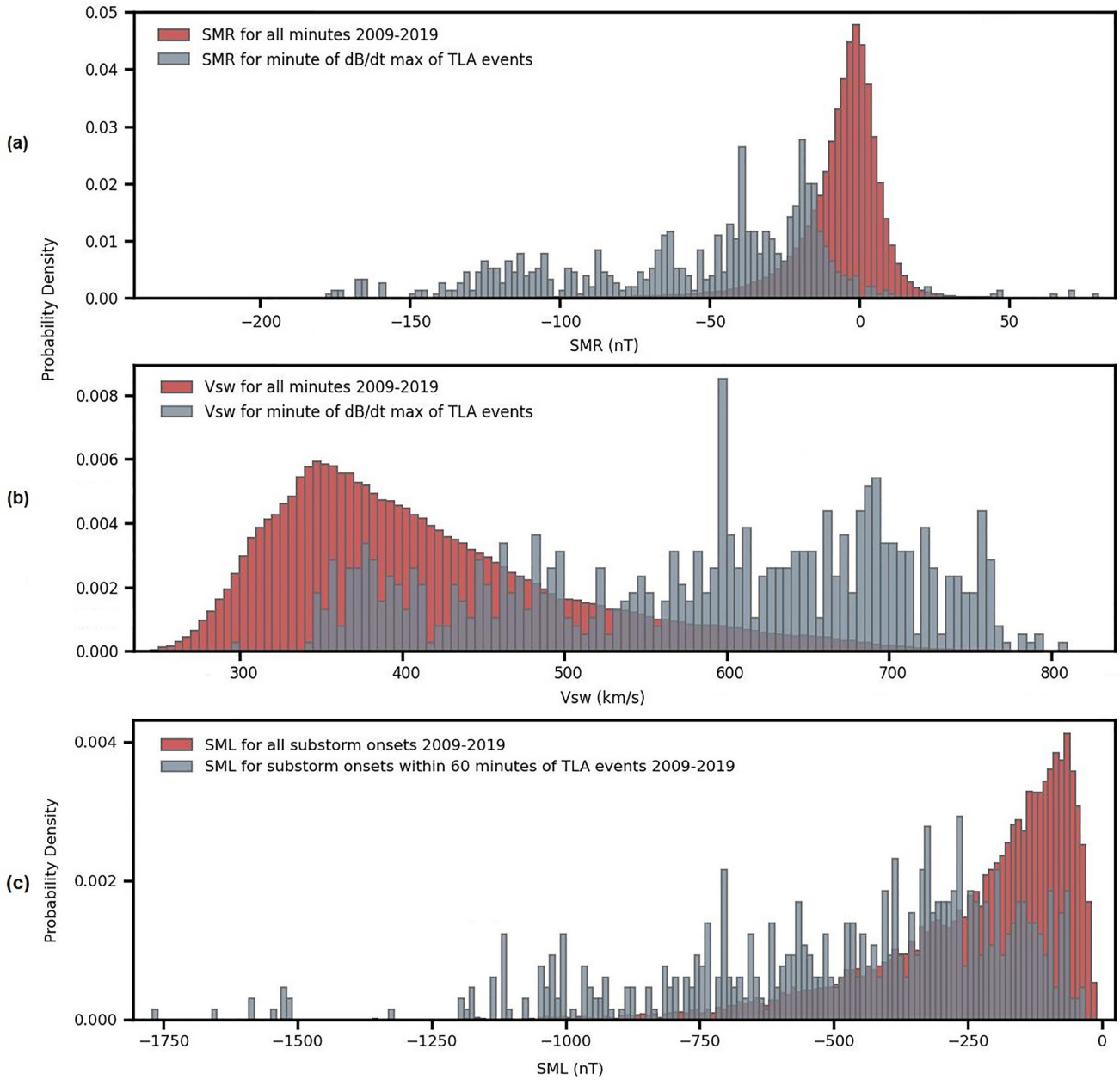

Figure 4. (a) Probability density of all SuperMAG ring (SMR) values throughout Solar Cycle 24 (pink) and probability density of SMR values during the minute of maximum dB/dt of each transient-large-amplitude (TLA) event throughout the solar cycle (blue). (b) Probability density of all Vsw values throughout Solar Cycle 24 (pink) and probability density of Vsw during the minute of maximum dB/dt of each TLA event throughout the solar cycle (blue). (c) Probability density of SML values for all substorm onsets throughout Solar Cycle 24 (pink) and probability density of SML values for substorm onsets that occurred within 1-hr of a TLA event (blue).

during each TLA event (blue). The Vsw values are from the OMNI database (time shifted to the Earth's bow shock nose; King & Papitashvili, 2020). These distributions show that Vsw peaks between 300 and 400 km/s, with a mean value of 412 km/s, and Vsw during TLA events is much higher on average (mean of 578 km/s) and a majority of values from 450 to 700 km/s.

Figure 4c shows the distribution of the SML values for the minute of substorm onset for all substorms that occurred from 2009 to 2019 (pink) and the SML values of the substorm onsets that occurred within 60 min of a TLA event (blue). The distribution of all substorm onset SML values has a mean of −234 nT and a σ of 189 nT, while the distribution of SML for substorm onsets that occurred within 1-hr of TLA events peaks for more negative SML with mean of −465 nT and a wider spread of SML with a σ of 316 nT. While Figure 3 shows that there

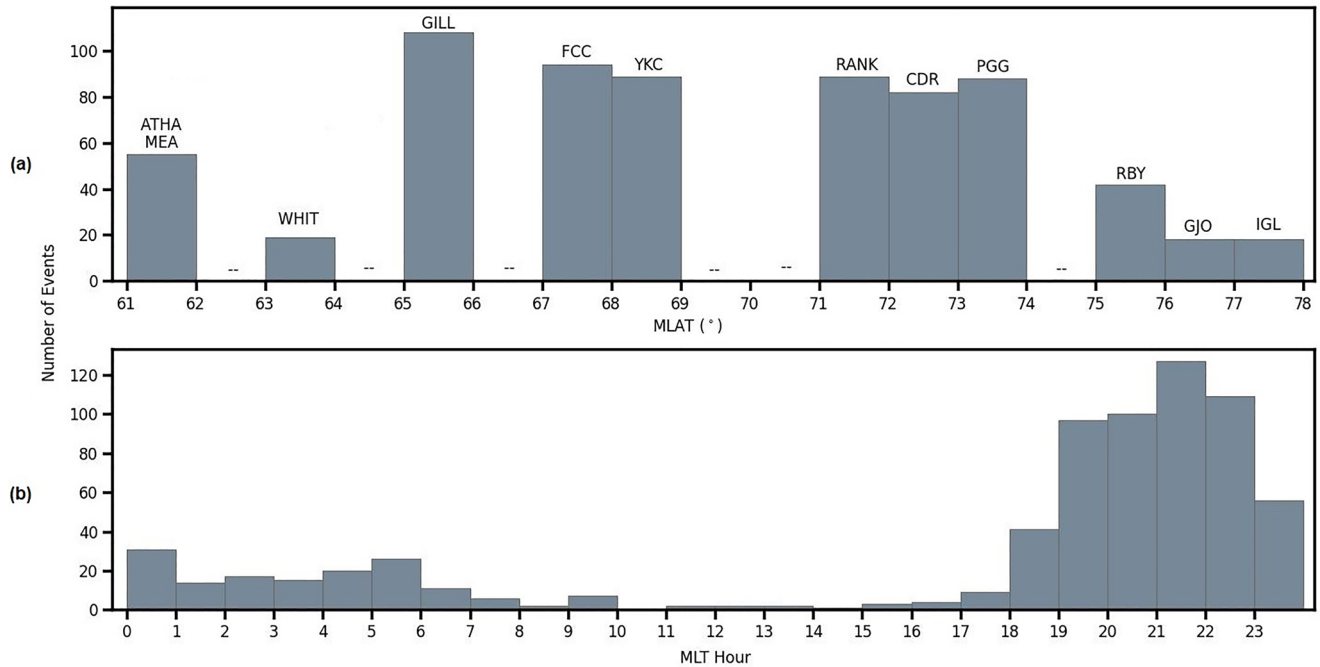

Figure 5. Histograms of (a) number of transient-large-amplitude (TLA) events based on magnetic latitude range and (b) number of TLA events that occurred for every hour of magnetic local time.

was often a larger number of TLA events during days when there was also a larger number of substorm onsets; Figure 4c shows that TLA events often occurred within 1 hr of substorm onsets with more negative SML values that is, more disturbed conditions of the westward electrojet (WEJ).

Figure 3 shows that TLA events occur more often during the declining phase of the solar cycle when substorm activity is increased and large geomagnetic storms driven by coronal mass ejections (CMEs) occur less often. This observation together with Figures 4a and 4b that show TLA events are more common during slightly elevated ring current activity and fast solar wind speeds may indicate that TLA events may be related to weak geomagnetic storms caused by coronal holes and subsequent corotating interaction regions (CIRs) that are most frequent in the descending phase (Hajra & Sunny, 2022) and give rise to fast flow speeds that can cause mild ring current activations.

5. Latitude and Local Time Dependence

In this section, we examine the latitude and magnetic local time (MLT) dependence of TLA events. For these purposes, a subset of the full database of TLA events was created so that there are an equal number of stations used from each magnetic latitude range. This subset consists of TLA events identified in all 12 stations for the years of 2015–2019 only (excluding the two AUTUMNX stations used in the event analysis of Section 7, see Table S1 in Supporting Information S1). There are three stations in each magnetic latitude range: 61°–64°, 65°–69°, 71°–74°, and 75°–78°. It is also important to note that we surveyed seven magnetometer stations in the midlatitude region from 30° to 60° MLAT and three stations in the equatorial region below 30° MLAT for all years of the solar cycle and we found no geophysical TLA signatures at any magnetic latitudes lower than 60°.

Figure 5 shows two distributions of the number of TLA events based on the magnetic latitude at which they occurred (a) and the MLT at which they occurred (b). The bars in Figure 5a each represent the number of events at each station except for the bar showing events from 61° to 62° that includes both the ATHA and MEA stations with very close separation distance. The degrees of magnetic latitude that show zero events do not necessarily indicate that zero TLA events occurred at those latitudes. Rather, these empty spaces signify the highly localized nature of TLA events and the need for a dense magnetometer network in order to detect them over all latitudes of the high-magnetic latitude region.

Figure 5a shows that a majority of TLA events occurred in the 65°–69° range with a slightly smaller population of events in the 71°–74° range. The equatorward boundary of the auroral oval is nominally around 65°; during the expansion phase of substorms the auroral oval can extend to 62°–64° and 68°–70° in the midnight sector (Akasofu, 1964).

Figure 5b shows the local time distribution of TLA events for each hour of MLT. This plot shows that TLA events are primarily nighttime events, with two distinct local time populations. The majority of events occurred from 17 to 01 MLT and a much smaller number of TLA events occurred from 01 to 08 MLT. About 3% of the total TLA events from 2015 to 2019 occurred during the daytime (referred to here as those occurring from 08 to 17 MLT, outside of the two nighttime populations). Daytime events were most commonly associated with geomagnetic storms (10 events were related to SCs, 5 occurred during the main phase and 2 during first day of recovery); however, 3 daytime events are referred to as unrelated events that were not associated with a storm and occurred more than 60 min from a substorm onset. Unrelated events, that occurred more than 60 min from substorm onset and in the absence of a CME-driven geomagnetic storm, comprised just over 8% of the TLA events that occurred in the 2015–2019 subset.

6. Connection to Substorms and GMD Events

McCuen et al. (2021) analyzed TLA events solely from five MACCS stations for the year of 2015 and showed that they were strongly associated with substorms and GMD events. Nighttime GMDs are magnetic perturbations with amplitudes of hundreds of nT and periods of 5–10 min (Engebretson et al., 2019a). These events are generally localized to a ∼275 km radius and they occur in two distinct local magnetic time populations in the pre- and post-midnight regions (Engebretson et al., 2019b). GMDs are often associated with substorm onsets but substorms are not necessary to cause them (Engebretson et al., 2021); the pre- and post-midnight populations show different temporal relations to onsets, indicating that there may be distinct M-I drivers for GMDs dependent on MLT.

Nighttime GMDs have been observed to coincide with dipolarizations in the magnetotail and subsequent auroral streamers (Engebretson et al., 2019b) as well as omega bands (Engebretson et al., 2020). The spherical elementary current system (SECS) analysis of nighttime GMDs by Weygand et al. (2021) found that a majority of GMDs occurred underneath the WEJ; many of the pre-midnight events occurred within the Harang current system while the remaining pre-midnight as well as many of the post-midnight events occurring underneath the downward region 1 or upward region 2 field-aligned current (FAC) systems.

In the present analysis, TLA events (from the same subset of TLA events used in Section 5 from 2015 to 2019 and excluding KJPK and SALU, see Table S1 in Supporting Information S1) are analyzed in comparison with a data set of GMD events (Engebretson, 2023) that consists of nighttime GMDs that occurred at the RBY, CDR, and PGG stations from 2015 to 2019. In this subset of GMD events, there are 843 hour windows in which GMDs occurred and 236 of them exhibited associated TLA dB/dt intervals. The most extreme GMD events with derivative amplitudes exceeding 12 nT/s occurred within 154 hour windows and of the 154 hour windows of extreme GMD events, a large majority (124 windows, 81%) have TLA dB/dt intervals included within the hour window. For GMDs with derivative amplitudes over 20 nT/s, this percentage is even higher: from 2015 to 2019, 28 hour windows included GMDs > 20 nT/s and 26 of these windows (93%) included TLA intervals as well.

Of those 124 hour windows with extreme GMDs and associated TLA dB/dt, there are 91 hour windows that consist of GMDs observed at multiple stations; 58 of these windows have the largest TLA dB/dt at the station location of the largest GMD. There are 78 cases of hour windows in which extreme GMDs occur at multiple stations and TLA dB/dt intervals occur at fewer station locations than the GMDs. In other words, TLA events were often even more localized than the spatial extent of the GMDs and further, when the nighttime GMDs commonly occurred at more than one station, the largest TLA dB/dt occurred at the specific location of the largest GMD.

To examine the relationship between substorms, nighttime GMDs, and TLA dB/dt events, Figure 6 shows the number of TLA and GMD events that occurred from 2015 to 2019 based on their temporal proximity from the nearest substorm onset (a) and the longitudinal difference of the TLA and GMD events from the location of the substorm onset (b). These substorm onset times and locations are from the SuperMAG substorm event list defined by Newell and Gjerloev (2011). Because TLA events often consist of multiple dB/dt signatures, the time and location of each event is marked with the maximum dB/dt interval of each TLA event. The blue bars

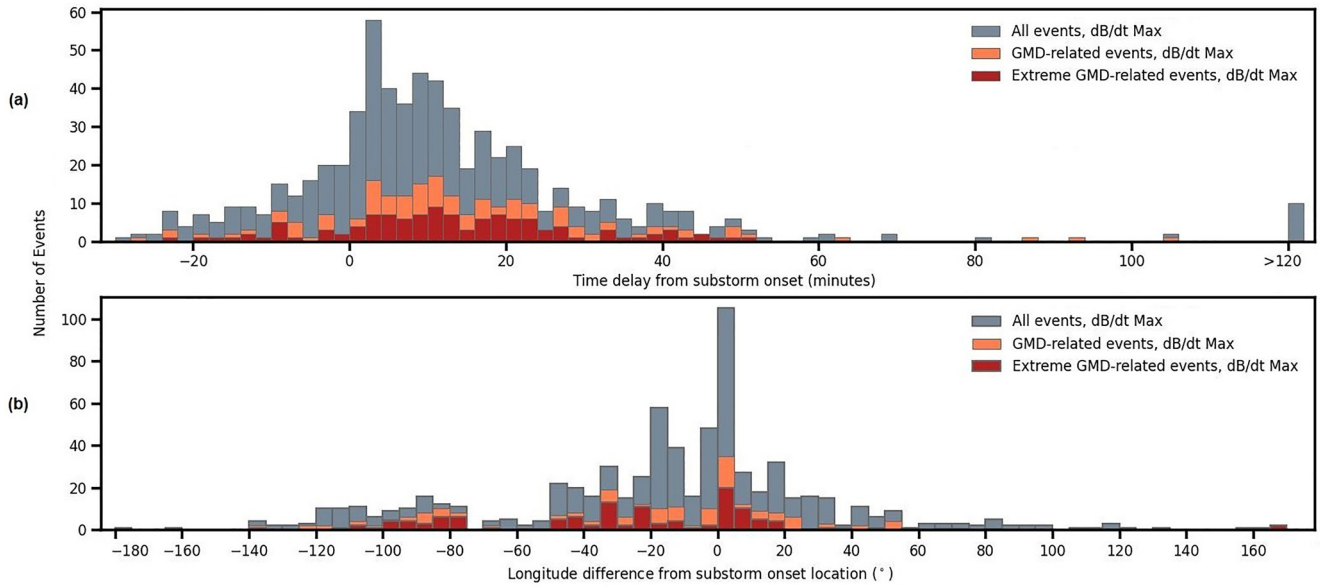

Figure 6. Number of 1-hr event windows from 2015 to 2019 that contain transient-large-amplitude (TLA) events (blue), TLA events related to geomagnetic disturbances (GMDs) (orange), and TLA events related to extreme GMDs (red) as a function of the time delay from substorm onset (a) and the longitude difference (in geographic coordinates) from where the TLA event occurred to where the substorm onset occurred (b).

in Figure 6 show the number of all TLA events, the orange bars show TLA events that were related to GMDs within the same hour window, and the red bars show the number of TLA events related to extreme GMD events (>12 nT/s).

Figure 6a shows that TLA events most commonly occur within 20 min of substorm onset with average onset delay of 5.5 min ($\sigma = 55.4$ min). TLA events also occurred in the 30 min prior to onset but much less frequently than 30 min after onset. The distribution of hour windows containing GMD-related TLA events is wider than that of the total TLA event population with an average delay of 7.9 min and σ of 72.6 min. Figure 6a shows that extreme GMD events with associated TLA intervals comprise about half of all GMD-related TLA events, meaning that when GMD events occur with associated TLA dB/dt they are very likely to be the most extreme GMD events. This distribution also shows that hour windows containing extreme GMD events with associated intervals can occur well beyond 20 min from the most recent substorm onset, and a sizable population of TLA intervals occur more than 2 hr from onset.

Figure 6b shows the number of hour windows that occurred for a given difference in longitude from the location of substorm onset identified by Newell and Gjerloev (2011) to the location of the maximum dB/dt of TLA events. Here, negative degrees of longitude difference signify that the location of the TLA and/or GMD events within the hour window occurred to the west of the location of the substorm onset. The distance conversion of longitudinal degrees to kilometers ranges from 65 km per 1° longitude at 54° geographic latitude (the geographic latitude of the lowest station) to 38 km per 1° longitude at 70° geographic latitude (geographic latitude of highest station), for an average of about 52 km per 1° longitude over this latitude range.

The distribution of Figure 6b shows that most TLA and TLA-related GMD events occurred within ±20° longitude of the substorm onset and more often occurred 20° to the west of the onset location rather than to the east. Further, Figure 6 shows that many hour windows containing extreme GMD events with associated TLA intervals occurred very far from the location of the substorm onset, in many cases more than 80° of longitude west of the onset location. Taken together, these two figures show that a majority of TLA events are closely related to substorm activity, but also shows the distinction that many TLA events, especially those related to extreme GMDs, can have in both time and space from substorm onsets.

7. Analysis of 30 September 2016 GMD/TLA Events

Figure 7 shows GMD events that occurred at six stations on 30 September 2016. The data for each station are plotted from top to bottom in order of decreasing magnetic latitude. Within these GMDs, TLA intervals occurred

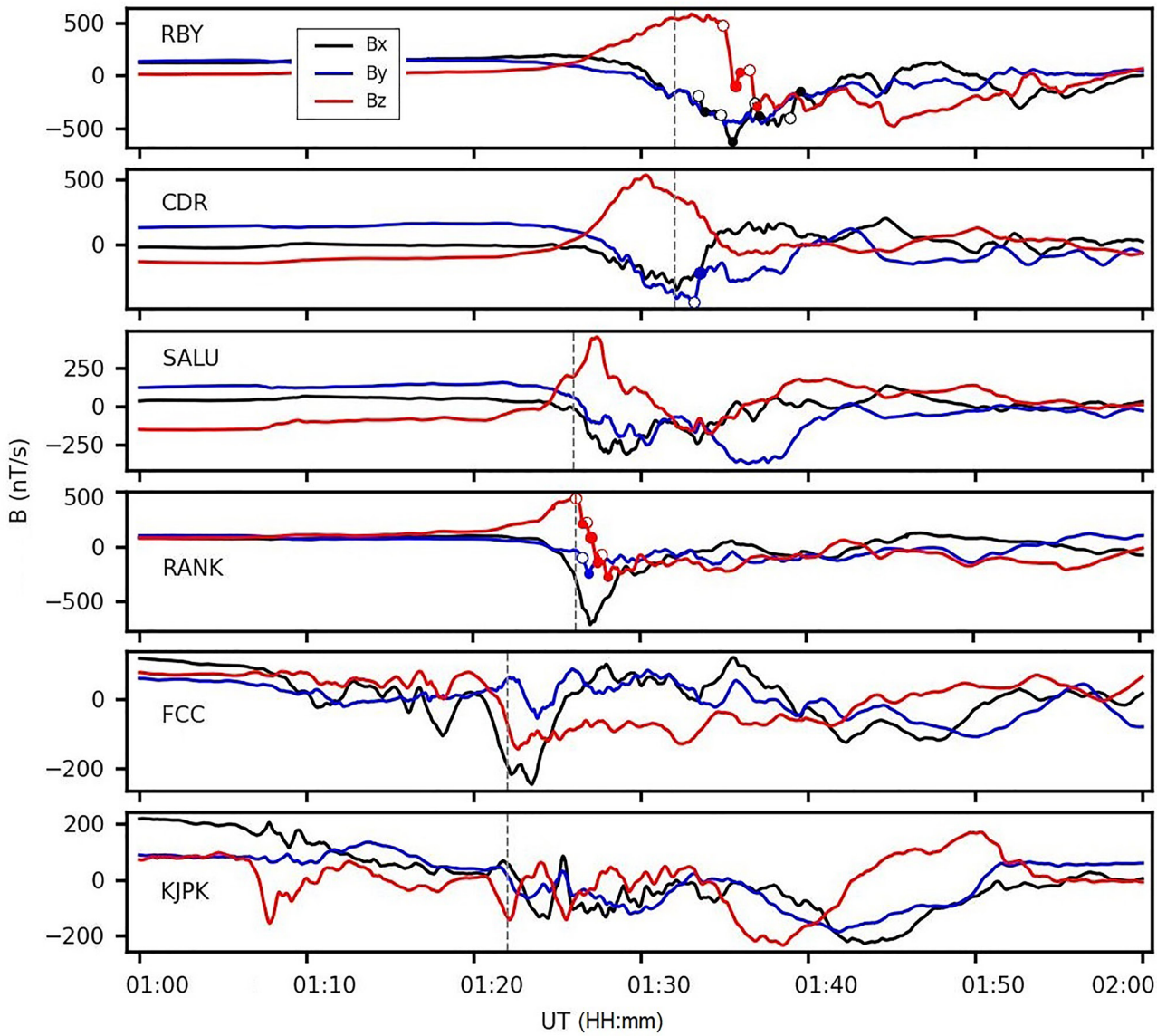

Figure 7. Magnetic field data from six stations on 30 September 2016. The Bx-component is displayed in black, By in blue, and Bz in red. The transient-large-amplitude (TLA) intervals that occurred within some of the events are signified by hollow circles denoting the start of the interval and filled circles denoting the end of the interval. The dashed vertical lines signify the times that correspond to the spherical elementary current system (SECS) maps in Figure 8. The mean *B* value in each component for the interval shown has been subtracted.

at the RBY, CDR, and RANK stations, shown as open circles signifying the start of each interval and solid circles as the end. The TLA intervals first occurred at the RANK station from 01:26 to 01:28 UT, at CDR within the 01:33 UT min, and then at RBY from 01:33 to 01:39 UT. The largest amplitude derivative (−12.29 nT/s) occurred at RBY in the *z*-component, lasting 44 s, and spanning the minutes from 01:34 to 01:35 UT. The GMDs at CDR, RBY, and SALU are all among very large events in the GMD database, with derivative amplitudes exceeding 12 nT/s.

This event occurred during moderate geomagnetic activity during what appears to be recovery from a CIR-driven storm (the SMR index reached −59 nT at 09:40 UT on 29 September, then recovered, and fluctuated between ∼−30 nT and −10 nT throughout 30 September). A substorm onset occurred at 01:10 according to the method of Newell and Gjerloev (2011). Substorm auroral onsets are determined by major auroral intensifications (Akasofu, 1964; Nishimura et al., 2010); by this definition, a small substorm auroral onset occurred at 01:05 UT and a larger onset occurred at 01:20 UT. The SML index increased ∼160 nT from 01:00 to 01:10 UT, then

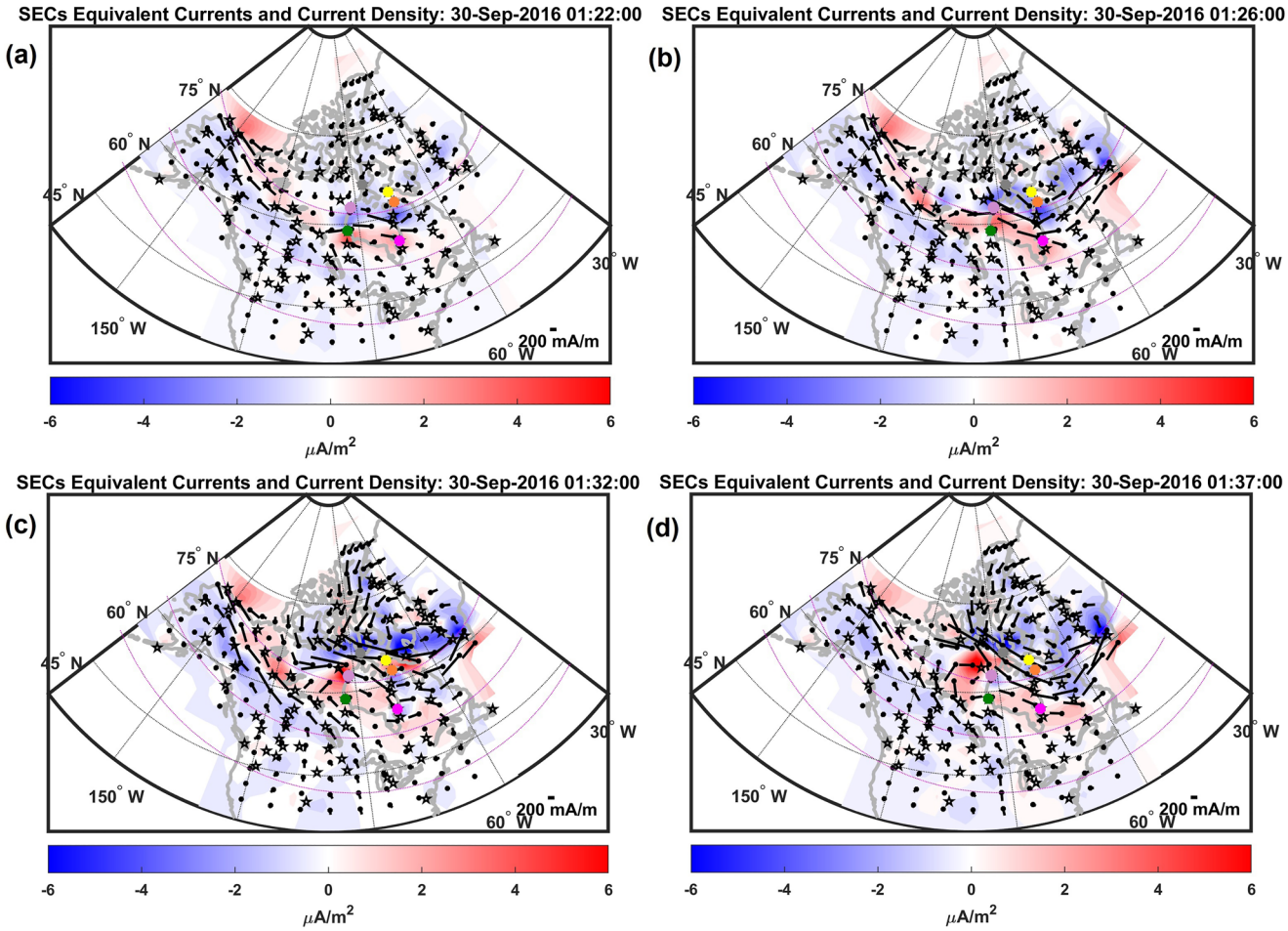

Figure 8. Four spherical elementary current system (SECS) maps during the 30 September 2016 event in geographic coordinates (dotted black lines) and geomagnetic coordinates (dotted pink lines). Each panel shows the combined field-aligned like current densities and equivalent currents. The dots indicate the points at which the equivalent current was determined and the vector gives the magnitude and direction. The stars mark the stations with useable data on that day. The key for the equivalent current is given in the lower right corner, and the color bar indicates the current density values. The colored circles mark CDR (yellow), RBY (gray), SALU (orange), RANK (mauve), FCC (green), and KJPK (pink).

decreased to the minimum value of −785 nT at 01:29 before increasing again to pre-onset values by the end of the hour, but did not show any distinction of the substorm auroral onset at 01:05 UT.

The average solar wind flow speed was 685 km/s and average solar wind dynamic pressure was around 2.4 nPa during this hour, both of which rose slightly at the time of onset (to 708 km/s and 2.8 nPa, respectively) and then returned to varying near the average. The IMF Bz (OMNI data time shifted to bow shock nose) turned southward (decreasing) from 01:05 to 01:21, 01:23 to 01:30, and 01:32 to 01:38 with sharp northward increases in between the intervals, then increased slowly at 01:38 for the remainder of the hour.

In order to analyze the ionospheric behavior during this interval, the SECSs method developed by Amm and Viljanen (1999) and applied to magnetometers in North America and Greenland by Weygand et al. (2011) was used to analyze the horizontal equivalent ionospheric currents and the vertical current amplitudes during this interval. Figure 8 displays SECS maps for pertinent minutes throughout this event, with the stations in Figure 7 marked as colored circles. The red shaded regions indicate locations of upward currents perpendicular to the ionosphere and the blue shaded regions indicate downward currents, with the degree of shading signifying the strength of the current. Further, Movie S1 shows a mosaic composition of images taken every 15 s from THEMIS All-Sky Imagers (ASIs) at four stations in this region for the hour interval in which this event occurs.

The two southern-most stations, FCC and KJPK, measured slight disturbances near the time of the substorm onset ~01:10 UT. The SECS map at 01:10–01:11 UT (not shown) indicates a slight and localized intensification

of the upward current and mild south-eastward horizontal currents above the FCC and GILL stations. At 01:22 (Figure 8a, and marked as a dashed line in the KJPK and FCC panels of Figure 7), an up–down current pair appeared spanning from East to West over Hudson Bay, shown in the SECS map of Figure 8a. At this time, the RANK and SALU stations (mauve and orange, respectively) are both underneath the downward R1 currents, and RANK and FCC both lie on the east side of the Harang current system. A moderate westward horizontal current is shown in the shear region between the up–down current pair. Magnetic disturbances were observed at FCC and KJPK near this time, most notably at FCC but not at the stations north of FCC.

At 01:26 (Figure 8b, and marked in RANK and SALU panels of Figure 7), the SECS maps show that the current pair begins to extend northward. GMDs were seen at RANK and SALU, with TLA intervals in the By- and Bz-component at RANK. At this time, SALU is still underneath the downward R1 currents, while RANK is located in the boundary region between downward and upward R1 currents. From about 01:26 to 01:28, strong WEJ currents are observed in the SECS maps extending over SALU that turn slightly northward to the north of RANK and southward to the south of RANK.

At 01:32–01:33 (Figure 8c, and marked in CDR and RBY panels of Figure 7), the upward portion of the current pair in red (to the south of the downward portion in blue) separates into two separate localized upward vertical current systems on either side of the north edge of the Hudson Bay. At this time, WNW horizontal currents are enhanced overhead of the upward current lobes. GMDs were recorded at the two northern-most stations, CDR and RBY, with peaks near 01:32–01:33 and TLA intervals in the x-component at CDR and x- and z-components at RBY. While there are large positive excursions in the z-components at both CDR and RBY around 01:33 UT, the SECS maps show that these disturbances appear to be caused by separate, localized upward systems overhead each station on either side of the northern Hudson Bay. Over the next 10 min from 01:32 to 01:42, the upward current on the east side weakens, while the upward current to the west moves slightly northwest and intensifies at 01:37 (Figure 8d) when TLA dB/dt are measured at RBY (Figure 7 top panel) before weakening at 01:39 when the GMDs at all of the four northern stations begin to subside.

The ASI data images in Movie S1 are consistent with the magnetic field data and SECS maps. A relatively stationary east-west auroral arc appeared just north of KJPK soon after the time of the first substorm auroral onset and extended across the bay over FCC by 01:18. The second substorm auroral onset started at 01:20 and initiated a series of brightenings. At 01:22, a poleward boundary intensification (PBI) began and the arc extended northward with auroral streamers that emerged from the arc at 01:26:30 in two distinct areas: (a) one to the west of SALU over RANK (where TLA dB/dt occur) and (b) another part to the south of SALU. Note that there are three stationary streaks of light in all of the ASI images at the SNKQ station (to the southeast of CDR, to the southeast of SALU, and directly south of PGG), these are stationary throughout the ASI movie and are artifacts rather than streamers.

The arc portion (a) over RANK continued moving poleward, while a streamer emerged at 01:26:30 UT and moved equatorward. This streamer can be seen in Figure 9 to the south of RANK. Then at 01:29:30, the arc broke up into a smaller part to the north and a longitudinally extending streamer to the south. The streamer north of RANK continued moving poleward and began to fade at 01:32, while the southern streamer moved equatorward and dissipated by 01:31.

The arc portion (b) south of SALU at 01:26:30 had two portions within it, one to the south and extending slightly west of SALU and a stronger part SE of SALU. By 01:27:30, these two features were more distinct, extending in the NW-SE direction. The part south of SALU reached SALU at 01:27:45, while the eastern part moved equatorward. Both portions then retreated equatorward and faded away by 01:29. At this same time, a new streamer appeared NE of SALU, intensified as it moved equatorward, and dissipated by 01:31. From 01:31:30, a small streamer appeared over RANK and moved equatorward while extending longitudinally at 01:32:30 and then fading. During this time, another intensification occurred NE of SALU and streamers moved equatorward, then faded by 01:35:45.

Figure 10 shows magnetic field data measured by the GOES-13 spacecraft during this event. The field-line footprint of GOES-13 at this time is shown in Figure 1. Here, Bz (plotted in red) is parallel to the Earth's rotation axis, positive northward, Bx is in the Earthward direction perpendicular to Bz, and By is in the eastward direction perpendicular to Bx and Bz. The sharp increases in Bz (highlighted as gray panels) signify dipolarization fronts (DFs) in the magnetotail at geosynchronous orbit (Ohtani et al., 2020), the timing of which coincide with the timing of ionospheric current enhancements and subsequent GMDs measured on the ground.

The first substorm auroral onset occurred at 01:05 UT and a second onset occurred at 01:20 UT, both with DFs that occurred ~2–3 min after. Perturbations were measured at the two southern-most stations, KJPK and FCC,

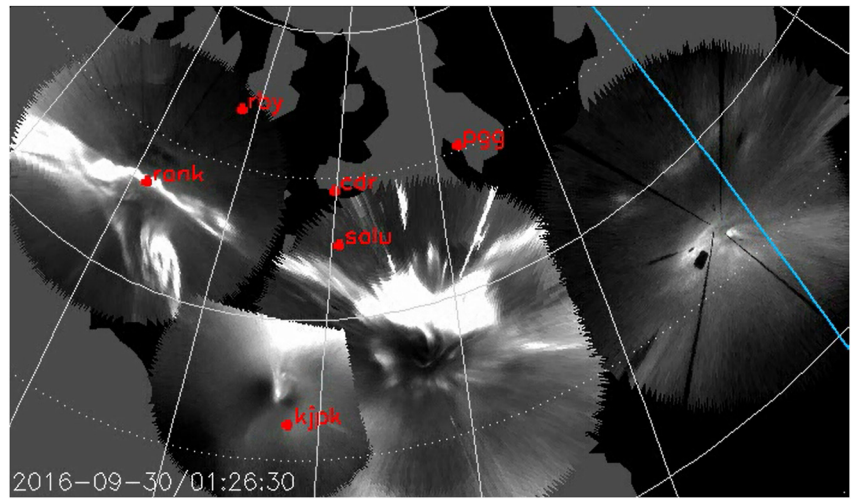

Figure 9. All-Sky Imager (ASI) image data from four stations at 01:26:30 UT showing separate streamers that have emerged from auroral arc south of RANK and south of SALU.

corresponding closely with these DFs. An east-west auroral arc appeared around 01:12 north of KJPK and south of SALU. The arc brightened around 01:22 after the second substorm onset and DF; the SECS maps show an E-W, up–down current pair extended across the southern Hudson Bay, westward horizontal currents increased in this region, and a GMD occurred at FCC. At about 01:26, a third DF occurred and the auroral arc began to move poleward and split into two separate parts over RANK and SALU, with auroral streamers that emerged from the arc and moved equatorward. The SECS maps show the up–down vertical current pair moved northward as well and the horizontal currents increased in the northwest direction; GMDs were observed at RANK and SALU with TLA intervals within the GMD at RANK, but not at SALU. Then around 01:33, another DF occurred at geosynchronous orbit as auroral patches were observed over RANK and SALU, developing into longitudinally localized streamers that moved equatorward; two distinct regions of localized upward vertical currents enhanced on either side of the northern Hudson Bay and strong WNW horizontal currents extended over the region. During this time, GMDs occurred at CDR and RBY, with TLA intervals within the GMDs at both stations.

The auroral poleward expansion shown in the ASI data corresponds well with the poleward progression of GMDs and the timing of the largest ionospheric currents. DFs are the leading edge of dipolarizing flux bundles (DFBs; Nakamura et al., 2002), defined as transient (~40 s), localized (<~$3R_E$ in X_{GSM} and Y_{GSM}) flux tubes carrying strong northward magnetic field (Liu et al., 2018). DFBs typically propagate at high speeds from the near-Earth reconnection region, efficiently transporting magnetic flux in short flow bursts referred to as bursty bulk flows (BBFs). Auroral streamers emerging from PBIs are considered to be the auroral signatures of BBFs (Henderson

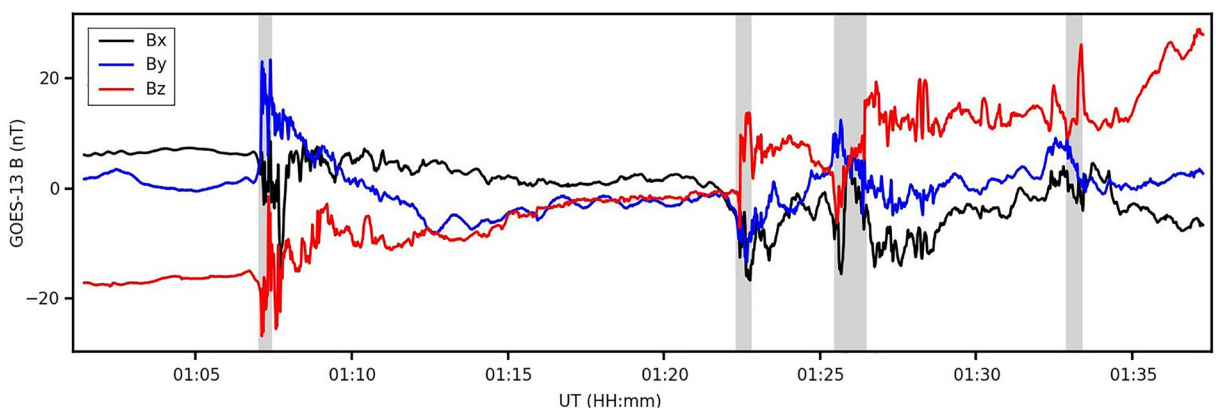

Figure 10. Magnetic field data measured by the GOES-13 spacecraft during the geomagnetic disturbance (GMD)/transient-large-amplitude (TLA) event. The average *B* value for the interval shown has been subtracted from each component.

et al., 1998; Sergeev et al., 1999). Although there is no available plasma flow velocity data in the magnetotail during this time, the DFs at GOES-13 in the magnetotail paired with the PBI and streamers in the ionosphere appear to be evidence of a BBF event. Further, the double auroral onset nature of this case may indicate that the first auroral onset was a pseudo-breakup: a small, localized, substorm-like activation of auroral brightening that often precedes a full-scale substorm. Pseudo-breakups can be associated with localized dipolarization in the tail that does not cause a global reconfiguration of the magnetotail (Akasofu, 1964) but can generate a localized current wedge (T. I. Pulkkinen, 1996; T. I. Pulkkinen et al., 1998).

We suggest that the cause of the poleward progression in this event is the tailward retreat of the magnetotail reconnection region due to successive DFBs. As the magnetic field dipolarizes, the reconnection region shifts downtail and this corresponds to the poleward shift of the larger magnetic footprint. Further, the Earthward propagation of fast flows in the plasma sheet causes the PBIs to extend equatorward and align in the north-south (NS) direction, forming auroral streamers (Ieda et al., 2016; Nakamura et al., 2011).

The overall structure of the GMDs are observed progressing northward; the peaks are measured closely in time for stations with similar magnetic latitudes, but the TLA intervals present are observed to be more longitudinally localized. For instance, RANK and SALU are about a degree separate in latitude and see relatively simultaneous peaks in all three components as the vertical current pair and auroral arc move northward, however TLA dB/dt are measured only at RANK. Then, CDR and RBY show a similar peaks in time but many more TLA intervals are observed at RBY than CDR. The stations on the western region of the Hudson Bay (RANK, RBY) where the localized upward current structure was stronger, exhibited the majority of TLA intervals in this event. It appears that while the GMDs at each station are a response to the larger-scale (roughly 1,000 km) ionospheric currents, the TLA dB/dt's are smaller-scale features of more localized FACs and auroral intensifications. Further, the SML index in this case does not reflect the timing of the TLA dB/dt that align fairly closely with the auroral enhancements and features of the SECS maps. This discrepancy is likely due to the localization and rapidity of the ionospheric variations causing the TLA dB/dt; the SME index uses 1-min cadence magnetic field data with a sliding 30-min buffer (Newell & Gjerloev, 2011) that may not capture the small-scale ionospheric enhancements.

8. Discussion

Engebretson et al. (2019b) analyzed three separate GMD events that occurred during 2015. It was shown that all three of these events occurred within 1-hr of a substorm onset as well as a dipolarization at GOES-13, indicating that these events were generally related to fast flows from the magnetotail that penetrated the near-Earth plasma sheet. These events all exhibited a northward and westward spatial progression, and SECS maps during these events showed coinciding regions of localized horizontal current enhancements with ∼275 km radius. Two of these three events had TLA dB/dt intervals within the GMD: Event 1 on 11 November 2015 and Event 3 on 9 October 2015. In Event 1, TLA events occurred at two of the four stations that measured GMDs and in Event 3, TLA dB/dts occurred at one of the four stations. In both Events 1 and 3, the locations of the GMDs that had associated TLA dB/dt are where the largest GMDs (>12 nT/s) occurred over the spatial extent of the disturbance; Event 2 exhibited no extreme GMDs and had no associated TLA signatures.

The TLA-related GMD events of the present study show some consistency with the spatial progression of those in Engebretson et al. (2019b): many TLA intervals occurred prior to the GMD at a more southern station (as shown in Figures 2 and 7) indicating northward progression of a fast ionospheric event. However, in comparison to substorm onsets, many TLA-related GMD events occurred to the west of the location of substorm onset defined by Newell and Gjerloev (2011), indicating an eastward progression in some cases. Rather than an eastward progression, this could be due to the overall northward progression of a larger ionospheric disturbance (i.e., poleward expansion of the WEJ [Olson & Rostoker, 1975]), but with more longitudinally localized variations (i.e., auroral streamers) causing the rapid TLA signatures at only some of the stations, as in the event analyzed in Section 7.

Wei et al. (2021) presented an analysis of intense dB/dt events on the ground that occurred on 7 January 2015. The perturbations occurred from 08:40 to 09:20 at 24 stations in midlatitude to high-latitude North America. During this event, large GMDs with TLA intervals within them occurred at SALU and KJPK. The study by Wei et al. (2021) included seven other stations that were also analyzed in the present study, and four of these stations exhibited TLA signatures (ATHA, MEA, GILL, and RANK, temporally in that order). The larger perturbations

and the TLA events showed a northward progression. This event occurred just after a substorm onset and in close temporal response to a BBF event carrying multiple DFs that were detected by the Cluster spacecraft in the inner magnetosphere ($\sim -4R_E$). It is suggested in Wei et al. (2021) that during this event, the large-scale SCW system is composed of multiple localized R1-sense FAC structures driven by multiple BBFs, as has been previously proposed (Birn & Hesse, 2014; Liu et al., 2013) and demonstrated (Liu et al., 2015, 2018).

Weygand et al. (2021) analyzed GMDs during 2015 and 2017 at CDR and KJPK and found that a majority of the events occurred within the WEJ and the pre-midnight events often occurred beneath the Harang current system. In Section 7, the pre-midnight event on 30 September 2016 is consistent with these observations: the SECS maps at 01:22 and 01:26 (Figures 8a and 8b) show that FCC and KJPK were within the upward Harang current with the WEJ flowing between this region and the downward Region 1 currents to the north, overhead RANK and SALU. Then at 01:32 UT, localized and transient upward vertical currents appear separately above RANK to the west and CDR to the east; the upward current lobe on the west strengthened near RBY when TLA dB/dt were measured at 01:37 UT. These localized vertical currents were likely FACs caused by DFBs in the inner plasma sheet, as evidenced by the dipolarization observed at GOES-13. The TLA dB/dt at RANK (01:26 UT) appeared when the station was located in a boundary region between upward and downward currents, as was the case for the TLA dB/dt that occurred at CDR near 01:32 UT and at RBY near 01:32 and 01:37 UT.

9. Summary and Conclusions

In this study, we have shown that TLA dB/dt events occurred primarily at night, preferentially in the pre-midnight sector. These high-frequency perturbations occurred only in the high-magnetic latitude region above 60° MLAT, with a majority in the 65°–74° MLAT band where substorm onset and expansion occurs. TLA events most often occurred within 60 min of substorm onsets but there is also a subset referred to as unrelated events that occurred more than 60 min after substorm onset and in the absence of a CME-driven geomagnetic storm. The large number of TLA events that occurred soon after substorm onset, in pre-midnight sector of the high-latitude region, suggests that these events are closely related to the upward portion of the SCW.

TLA dB/dt events occurred most often during the declining phase of the solar cycle when the yearly mean sunspot number decreases but the number of substorm onsets per year increases from solar maximum. TLA events are most common during intervals of mild SMR current activity and fast solar wind flow speeds. This may indicate a relationship between TLA and GMD events with weak CIR-driven storms due to fast solar wind flow speeds emanating from coronal holes. Future work includes an investigation of this potential association, especially for the so-called unrelated TLA events.

We have shown in this study that many TLA events during 2015–2019 were associated with GMDs, often preceding the event or occurring within the overall disturbance. Not only were TLA-related GMD events common, but as GMD amplitudes increased, the likelihood that TLA intervals were associated with the GMD vastly increased: 81% of hour windows with extreme >12 nT/s GMDs had associated TLA intervals, and 93% of even larger GMDs >20 nT/s included TLA intervals. Engebretson et al. (2019a, 2019b, 2021), and Weygand et al. (2021) all show that GMDs have an effective radius of ∼300 km. The results presented here show that high-frequency intervals of the magnetic field can be even more localized: TLA dB/dt intervals often occurred at fewer stations than the extent of the GMDs were measured, as shown in Figure 2 (17 December 2017), the event on 30 September 2016, Events 1 and 3 of Engebretson et al. (2019b) and the 7 January 2015 event of Wei et al. (2021). While TLA dB/dt are commonly more localized than GMD events, the locations of the largest TLA most often signify the locations of the largest GMDs.

This study has presented multiple cases of TLA dB/dt correlated with dipolarizations in the inner magnetosphere, as well as localized FAC structures, PBIs, and auroral streamers; one of which also included measurements of bursty Earth-directed plasma flows in the magnetotail (Wei et al., 2021). We show that TLA events are closely associated with substorm activity, but they also occur many tens of minutes and even hours apart from substorm onsets, as well as in locations very far from the location of the onsets. The spatial and temporal separation of some TLA events from substorms indicates that TLA events are driven by M-I processes that are often, but not always related to substorms. Additionally, TLA events may be the ground manifestations of highly localized pseudo-breakups and/or localized substorm current wedgelets driven by individual closed-field-line DFBs as in Liu et al. (2015, 2018). Because of their potential M-I source mechanisms and their subsequent relationship to

larger, longer GMDs on the ground, TLA events are relevant to GIC-driving processes but they are not always directly reflected in large-scale geomagnetic activity indices like SML that are derived with 1-min magnetic field data.

Strong magnetic perturbations and Pi 2 pulsations are closely correlated with auroral intensifications followed by streamers driven by DFs and fast flow bursts in the magnetotail (Kepko & Kivelson, 1999; Lyons et al., 2012; Nishimura et al., 2012). This study has shown that disturbances in the Pi 1 frequency range are often present in these situations as well. TLA magnetic perturbations appear to have complex M-I drivers, but they are likely the result of small-scale ionospheric current phenomena coupled to the magnetotail that often but do not always occur during substorms. Because these high-frequency signatures are very often associated with the most extreme nighttime GMDs that can drive GICs on Earth (and even though magnetic variations with Pi 1 and short Pi 2 periods do not drive GICs directly), TLA dB/dt and the associated M-I phenomena such as BBFs are important to take into account when investigating the complex dynamics that can give rise to GIC. Future work includes a broader investigation of the ionospheric currents, magnetotail dynamics—especially fast plasma flows in the tail—and solar wind drivers of TLA-related GMD events. Identification and analysis of TLA dB/dt in association with nighttime GMDs will continue to provide insight on their M-I drivers and their behavior from the ionosphere to the ground, where GMDs with associated TLA intervals pose the greatest threat of hazardous GICs.

Acknowledgments
This work was supported by NSF Grants 2013433 and 1848724, NASA Grant 80NSSC20K1779 to the University of Michigan, and by NSF Grant 2013648 to Augsburg University. This work at Boston University was supported by NASA Grants 80NSSC18K0657, 80NSSC21K1321, and 80NSSC22K0323, NSF Grants AGS-1907698 and AGS-2100975, and AFOSR Grant FA9559-16-1-0364. The authors thank the MACCS team for data, available at http://space.augsburg.edu/maccs/. The authors thank I. R. Mann, D. K. Milling, and the rest of the CARISMA team for data. CARISMA is operated by the University of Alberta, funded by the Canadian Space Agency. Data available at http://www.carisma.ca/. The authors thank the Geological Survey of Canada (GSC). CANMOS data can be found at https://geomag.nrcan.gc.ca/obs/canmos-en.php. We thank the Canadian Space Agency for support of AUTUMNX, data available at https://autumn.athabascau.ca/. We acknowledge NASA contract NAS5-02099 and V. Angelopoulos for use of data from the THEMIS Mission (available at http://themis.ssl.berkeley.edu). Specifically: S. Mende and C. T. Russell for use of the GMAG data and NSF for support through Grant AGS-1004814; S. Mende and E. Donovan for use of the ASI data, the CSA for logistical support in fielding and data retrieval from the GBO stations, and NSF for support of GIMNAST through Grant AGS-1004736. The magnetic footprint of GOES-13 was determined using tools provided by SSCWEB (https://sscweb.gsfc.nasa.gov/). The OMNI data were obtained from the GSFC/SPDF OMNIWeb interface at https://omniweb.gsfc.nasa.gov. GOES magnetometer data are available online (https://satdat.ngdc.noaa.gov/sem/goes/data/full/). We gratefully acknowledge the SuperMAG collaborators (https://supermag.jhuapl.edu/info/?page=acknowledgement).

Data Availability Statement

The database of TLA events is available on the University of Michigan Deep Blue Data Repository (doi.org/10.7302/9par-f788). The GMD event data are also available on UM Deep Blue (doi.org/10.7302/275e-da06).

References

Akasofu, S. I. (1964). The development of the auroral substorm. *Planetary and Space Science*, *12*(4), 273–282. https://doi.org/10.1016/0032-0633(64)90151-5

Amm, O., & Viljanen, A. (1999). Ionospheric disturbance magnetic field continuation from the ground to the ionosphere using spherical elementary current systems. *Earth, Planets Space*, *51*(6), 431–440. https://doi.org/10.1186/bf03352247

Arnoldy, R. L., Rajashekar, R., Cahill, L. J., Engebretson, M. J., Rosenberg, T. J., & Mende, S. B. (1987). Simultaneous measurement of aurora-related, irregular magnetic pulsations at northern and southern high latitudes. *Journal of Geophysical Research*, *92*(A11), 12221–12232. https://doi.org/10.1029/JA092iA11p12221

Atkinson, G. (1967). The current system of geomagnetic bays. *Journal of Geophysical Research*, *72*(23), 6063–6067. https://doi.org/10.1029/JZ072i023p06063

Belakhovsky, V., Pilipenko, V., Engebretson, M., Sakharov, Y., & Selivanov, V. (2019). Impulsive disturbances of the geomagnetic field as a cause of induced currents of electric power lines. *Journal of Space Weather and Space Climate*, *9*, A18. https://doi.org/10.1051/swsc/2019015

Birn, J., & Hesse, M. (2014). The substorm current wedge: Further insights from MHD simulations. *Journal of Geophysical Research: Space Physics*, *119*, 3503–3513. https://doi.org/10.1002/2014JA019863

Boteler, D. H., Pirjola, R. J., & Nevanlinna, H. (1998). The effects of geomagnetic disturbances on electrical systems at the Earth's surface. *Advances in Space Research*, *22*(1), 17–27. https://doi.org/10.1016/S0273-1177(97)01096-X

Connors, M., Schofield, I., Reiter, K., Chi, P. J., Rowe, K. M., & Russell, C. T. (2016). The AUTUMNX magnetometer meridian chain in Québec, Canada. *Earth, Planets and Space*, *68*(1), 2. https://doi.org/10.1186/s40623-015-0354-4

Engebretson, M. J. (2023). Solar cycle dependence of very large nighttime geomagnetic disturbances (GMDs) observed in Eastern Arctic Canada: Data [Dataset]. University of Michigan - Deep Blue Data. https://doi.org/10.7302/275e-da06

Engebretson, M. J., Cahill, L. J., Arnoldy, R. L., Mende, S. B., & Rosenberg, T. J. (1983). Correlated irregular magnetic pulsations and optical emissions observed at Siple Station, Antarctica. *Journal of Geophysical Research*, *88*(A6), 4841–4852. https://doi.org/10.1029/JA088iA06p04841

Engebretson, M. J., Hughes, W. J., Alford, J. L., Zesta, E., Cahill, L. J., Arnoldy, R. L., & Reeves, G. D. (1995). Magnetometer Array for Cusp and Cleft Studies observations of the spatial extent of broadband ULF magnetic pulsations at cusp/cleft latitudes. *Journal of Geophysical Research*, *100*(A10), 19371–19386. https://doi.org/10.1029/95JA00768

Engebretson, M. J., Kirkevold, K. R., Steinmetz, E. S., Pilipenko, V. A., Moldwin, M. B., McCuen, B. A., et al. (2020). Interhemispheric comparisons of large nighttime magnetic perturbation events relevant to GICs. *Journal of Geophysical Research: Space Physics*, *125*, e2020JA028128. https://doi.org/10.1029/2020JA028128

Engebretson, M. J., Pilipenko, V. A., Ahmed, L. Y., Posch, J. L., Steinmetz, E. S., Moldwin, M. B., et al. (2019a). Nighttime magnetic perturbation events observed in Arctic Canada: 1. Survey and statistical analysis. *Journal of Geophysical Research: Space Physics*, *124*, 7442–7458. https://doi.org/10.1029/2019JA026794

Engebretson, M. J., Pilipenko, V. A., Steinmetz, E. S., Moldwin, M. B., Connors, M. G., Boteler, D. H., et al. (2021). Nighttime magnetic perturbation events observed in Arctic Canada: 3. Occurrence and amplitude as functions of magnetic latitude, local time, and magnetic disturbance indices. *Space Weather*, *19*, e2020SW002526. https://doi.org/10.1029/2020SW002526

Engebretson, M. J., Steinmetz, E. S., Posch, J. L., Pilipenko, V. A., Moldwin, M. B., Connors, M. G., et al. (2019b). Nighttime magnetic perturbation events observed in Arctic Canada: 2. Multiple-instrument observations. *Journal of Geophysical Research: Space Physics*, *124*, 7459–7476. https://doi.org/10.1029/2019JA026797

Hajra, R., & Sunny, J. V. (2022). Corotating interaction regions during Solar Cycle 24: A study on characteristics and geoeffectiveness. *Solar Physics*, *297*(3), 30. https://doi.org/10.1007/s11207-022-01962-1

Henderson, M. G., Reeves, G. D., & Murphree, J. S. (1998). Are north-south aligned auroral structures an ionospheric manifestation of bursty bulk flows? *Geophysical Research Letters*, *25*(19), 3737–3740. https://doi.org/10.1029/98GL02692

Ieda, A., Nishimura, Y., Miyashita, Y., Angelopoulos, V., Runov, A., Nagai, T., et al. (2016). Stepwise tailward retreat of magnetic reconnection: THEMIS observations of an auroral substorm. *Journal of Geophysical Research: Space Physics*, *121*, 4548–4568. https://doi.org/10.1002/2015JA022244

Jacobs, J. A., Kato, Y., Matsushita, S., & Troitskaya, V. A. (1964). Classification of geomagnetic micropulsations. *Journal of Geophysical Research*, *69*(1), 180–181. https://doi.org/10.1029/JZ069i001p00180

Kappenman, J. G. (2006). Great geomagnetic storms and extreme impulsive geomagnetic field disturbance events—An analysis of observational evidence including the great storm of May 1921. *Advances in Space Research*, *38*(2), 188–199. https://doi.org/10.1016/j.asr.2005.08.055

Kataoka, R., & Ngwira, C. (2016). Extreme geomagnetically induced currents. *Progress in Earth and Planetary Science*, *3*(1), 23. https://doi.org/10.1186/s40645-016-0101-x

Kepko, L., & Kivelson, M. (1999). Generation of Pi2 pulsations by bursty bulk flows. *Journal of Geophysical Research*, *104*(A11), 25021–25034. https://doi.org/10.1029/1999JA900361

King, J., & Papitashvili, N. E. (2020). OMNI 1-min data set [Dataset]. NASA Space Physics Data Facility. https://doi.org/10.48322/45bb-8792

Lessard, M. R., Lund, E. J., Jones, S. L., Arnoldy, R. L., Posch, J. L., Engebretson, M. J., & Hayashi, K. (2006). Nature of Pi1B pulsations as inferred from ground and satellite observations. *Geophysical Research Letters*, *33*, L14108. https://doi.org/10.1029/2006GL026411

Lester, M., Hughes, J. W., & Singer, H. J. (1983). Polarization patterns of Pi 2 magnetic pulsations and the substorm current wedge. *Journal of Geophysical Research*, *88*(A10), 7958–7966. https://doi.org/10.1029/JA088iA10p07958

Liu, J., Angelopoulos, V., Chu, X., Zhou, X. Z., & Yue, C. (2015). Substorm current wedge composition by wedgelets. *Geophysical Research Letters*, *42*, 1669–1676. https://doi.org/10.1002/2015GL063289

Liu, J., Angelopoulos, V., Runov, A., & Zhou, X. Z. (2013). On the current sheets surrounding dipolarizing flux bundles in the magnetotail: The case for wedgelets. *Journal of Geophysical Research: Space Physics*, *118*, 2000–2020. https://doi.org/10.1002/jgra.50092

Liu, J., Angelopoulos, V., Yao, Z., Chu, X., Zhou, X. Z., & Runov, A. (2018). The current system of dipolarizing flux bundles and their role as wedgelets in the substorm current wedge (pp. 323–337).

Lyons, L. R., Nishimura, Y., Xing, X., Runov, A., Angelopoulos, V., Donovan, E., & Kikuchi, T. (2012). Coupling of dipolarization front flow bursts to substorm expansion phase phenomena within the magnetosphere and ionosphere. *Journal of Geophysical Research*, *117*, A02212. https://doi.org/10.1029/2011JA017265

Mann, I. R., Milling, D. K., Rae, I. J., Ozeke, L. G., Kale, A., Kale, Z. C., et al. (2008). The upgraded CARISMA magnetometer array in the THEMIS era. *Space Science Reviews*, *141*(1–4), 413–451. https://doi.org/10.1007/s11214-008-9457-6

McCuen, B. A. (2023). A statistical analysis of high-frequency transient-large-amplitude geomagnetic disturbances: Data [Dataset]. University of Michigan - Deep Blue Data. https://doi.org/10.7302/9par-f788

McCuen, B. A., Moldwin, M. B., & Engebretson, M. (2021). Characterization of transient-large-amplitude geomagnetic perturbation events. *Geophysical Research Letters*, *48*, e2021GL094076. https://doi.org/10.1029/2021GL094076

McCuen, B. A., Moldwin, M. B., Steinmetz, E. S., & Engebretson, M. J. (2023). Automated high-frequency geomagnetic disturbance classifier: A machine learning approach to identifying noise while retaining high-frequency components of the geomagnetic field. *Journal of Geophysical Research: Space Physics*, *128*, e2022JA030842. https://doi.org/10.1029/2022JA030842

McPherron, R. L., Russell, C. T., & Aubry, M. P. (1973). Satellite studies of magnetospheric substorms on August 15, 1968: 9. Phenomenological model for substorms. *Journal of Geophysical Research*, *78*(16), 3131–3149. https://doi.org/10.1029/JA078i016p03131

Nakamura, R., Baumjohann, W., Klecker, B., Bogdanova, Y., Balogh, A., Rème, H., et al. (2002). Motion of the dipolarization front during a flow burst event observed by cluster. *Geophysical Research Letters*, *29*(20), 1942. https://doi.org/10.1029/2002GL015763

Nakamura, R., Baumjohann, W., Panov, E., Petrukovich, A. A., Angelopoulos, V., Volwerk, M., et al. (2011). Flux transport, dipolarization, and current sheet evolution during a double-onset substorm. *Journal of Geophysical Research*, *116*, A00I36. https://doi.org/10.1029/2010JA015865

Newell, P. T., & Gjerloev, J. W. (2011). Evaluation of SuperMAG auroral electrojet indices as indicators of substorms and auroral power. *Journal of Geophysical Research*, *116*, A12211. https://doi.org/10.1029/2011JA016779

Newell, P. T., & Gjerloev, J. W. (2012). SuperMAG-based partial ring current indices. *Journal of Geophysical Research*, *117*, A05215. https://doi.org/10.1029/2012JA017586

Ngwira, C. M., Pulkkinen, A. A., Bernabeu, E., Eichner, J., Viljanen, A., & Crowley, G. (2015). Characteristics of extreme geoelectric fields and their possible causes: Localized peak enhancements. *Geophysical Research Letters*, *42*, 6916–6921. https://doi.org/10.1002/2015GL065061

Nikitina, L., Trichtchenko, L., & Boteler, D. H. (2016). Assessment of extreme values in geomagnetic and geoelectric field variations for Canada. *Space Weather*, *14*, 481–494. https://doi.org/10.1002/2016SW001386

Nishimura, Y., Lyons, L., Zou, S., Angelopoulos, V., & Mende, S. (2010). Substorm triggering by new plasma intrusion: THEMIS All-Sky Imager observations. *Journal of Geophysical Research*, *115*, A07222. https://doi.org/10.1029/2009JA015166

Nishimura, Y., Lyons, L. R., Kikuchi, T., Angelopoulos, V., Donovan, E., Mende, S., et al. (2012). Formation of substorm Pi2: A coherent response to auroral streamers and currents. *Journal of Geophysical Research*, *117*, A09218. https://doi.org/10.1029/2012JA017889

Ohtani, S., Motoba, T., Takahashi, K., & Califf, S. (2020). Generalized substorm current wedge model: Two types of dipolarizations in the inner magnetosphere. *Journal of Geophysical Research: Space Physics*, *125*, e2020JA027890. https://doi.org/10.1029/2020JA027890

Olson, J. V., & Rostoker, G. (1975). Pi 2 pulsations and the auroral electrojet. *Planetary and Space Science*, *23*(8), 1129–1139. https://doi.org/10.1016/0032-0633(75)90163-4

Pulkkinen, T. I. (1996). Pseudobreakup or substorm? In *3rd International Conference on Substorms* (pp. 285–293).

Pulkkinen, T. I., Baker, D. N., Wiltberger, M., Goodrich, C., Lopez, R. E., & Lyon, J. G. (1998). Pseudobreakup and substorm onset: Observations and MHD simulations compared. *Journal of Geophysical Research*, *103*(A7), 14847–14854. https://doi.org/10.1029/97JA03244

Pulkkinen, A., Bernabeu, E., Eichner, J., Viljanen, A., & Ngwira, C. (2015). Regional-scale high-latitude extreme geoelectric fields pertaining to geomagnetically induced currents. *Earth, Planets and Space*, *67*(1), 93. https://doi.org/10.1186/s40623-015-0255-6

Pulkkinen, A., Bernabeu, E., Thomson, A., Viljanen, A., Pirjola, R., Boteler, D., et al. (2017). Geomagnetically induced currents: Science, engineering, and applications readiness. *Space Weather*, *15*, 828–856. https://doi.org/10.1002/2016SW001501

Russell, C. T., Chi, P. J., Dearborn, D. J., Ge, Y. S., Kuo-Tiong, B., Means, J. D., et al. (2008). THEMIS ground-based magnetometers. *Space Science Reviews*, *141*(1–4), 389–412. https://doi.org/10.1007/s11214-008-9337-0

Sergeev, V. A., Liou, K., Meng, C. I., Newell, P. T., Brittnacher, M., Parks, G., & Reeves, G. D. (1999). Development of auroral streamers in association with localized impulsive injections to the inner magnetotail. *Geophysical Research Letters*, *26*(3), 417–420. https://doi.org/10.1029/1998GL900311

Wei, D., Dunlop, M. W., Yang, J., Dong, X., Yu, Y., & Wang, T. (2021). Intense *dB/dt* variations driven by near-Earth bursty bulk flows (BBFs): A case study. *Geophysical Research Letters*, *48*, e2020GL091781. https://doi.org/10.1029/2020GL091781

Weygand, J. M., Amm, O., Viljanen, A., Angelopoulos, V., Murr, D., Engebretson, M. J., et al. (2011). Application and validation of the spherical elementary currents systems technique for deriving ionospheric equivalent currents with the North American and Greenland ground magnetometer arrays. *Journal of Geophysical Research*, *116*, A03305. https://doi.org/10.1029/2010JA016177

Weygand, J. M., Engebretson, M. J., Pilipenko, V. A., Steinmetz, E. S., Moldwin, M. B., Connors, M. G., et al. (2021). SECS analysis of nighttime magnetic perturbation events observed in Arctic Canada. *Journal of Geophysical Research: Space Physics*, *126*, e2021JA029839. https://doi.org/10.1029/2021JA029839